(Received 12 August 2025, Accepted 26 November 2025, Scheduled 29 November 2025)

Variational Quantum Algorithm for Photonic Crystals

Long Chen[1,2,†], Xin Yu Li[1,2,†], Jian Lin Su[1,2,†], Si Qi Huang[1,2], Zi Xuan Cai[1,2], Zhi Cai Yu[1,2], Yu Ming Ning[1,2], Qiang Xiao[1,2], Jia Nan Zhang[1,2], Qian Ma[1,2], Zhihao Lan[1,2,*], Jian Wei You[1,2,*], and Tie Jun Cui[1,2,*]

[1] *State Key Laboratory of Millimeter Waves, Southeast University, Nanjing 210096, China*
[2] *Institute of Electromagnetic Space, Southeast University, Nanjing 210096, China*
[3] *Department of Electronic and Electrical Engineering, University College London, London WC1E 7JE, United Kingdom*

ABSTRACT: Photonic crystals (PhCs) play a crucial role in describing the quantized collective behavior of wave functions. However, the existing investigations into their eigenstates primarily rely on classical computational methods. Variational quantum algorithm (VQA) represents a promising quantum computing technology that can be implemented on noisy intermediate-scale quantum (NISQ) devices, potentially surpassing the classical computational capabilities. Here, we propose a method to analyze the band and eigenstate properties of PhCs based on variational quantum eigensolver (VQE). We firstly reformulate the Maxwell's equations into a Hermitian generalized eigenvalue problem. By appropriately selecting a loss function and employing the proposed quantum eigenvalue solver, we successfully obtain the generalized eigenvalues using a quantum gradient descent algorithm. To validate our approach, we perform simulations on two prototypical PhCs in square and hexagonal lattices. The results demonstrate that a complex *Ansatz* can effectively capture the optimal solution, successfully yielding the generalized eigenvalues, but a simpler *Ansatz* exhibits significant limitations. Our findings provide new insights into the application of VQAs in PhCs and other quantum topological systems.

1. INTRODUCTION

With the discovery of quantum Hall effect [1–4] and recent advancements in the study of topological insulators [5–9], the topological phases of matter have garnered significant attention within the realm of condensed matter physics. In 2008, Haldane and Raghu [10] successfully transferred the key features of the quantum Hall effect from electronic systems to classical electromagnetism, a groundbreaking theoretical framework that was subsequently verified through extensive numerical simulations and experimental studies based on magneto-optical photonic crystals (PhCs) [11, 12]. Following this pivotal work, topological PhCs [13, 14] have become a focal point of research due to their unique properties, particularly the transport phenomena of topologically protected edge states (i.e., electromagnetic wave modes that propagate unidirectionally at the material boundaries and are immune to disorder scattering) [15–17]. This phenomenon can be elucidated using topological invariants, such as the Chern number — an integer quantum number that characterizes the overall topological properties of the band structure, analogous to quantized Hall conductivity. These invariants are used to describe the bulk properties of materials [20–22]. Specifically, a non-zero Chern number indicates that the bulk states exhibit topological nontriviality, and according to the bulk-boundary correspondence principle, the system's boundaries must host gapless topological edge states. The role of these edge states is analogous to the classification of topological invariants in mathematics, highlighting their significance in understanding the behavior of complex systems.

Given the growing interest in the computational investigation of PhCs, it has become essential to explore methods that allow for efficient characterization of their properties. However, current research predominantly relies on classical computational techniques [23], and attempts to leverage the power of quantum computing remain largely unexplored. Variational quantum algorithms (VQAs) [18–28], which utilize parameterized quantum circuits in conjunction with classical optimizers, present a promising avenue for addressing these challenges, especially in the context of noisy intermediate-scale quantum (NISQ) devices [29–31]. A central mission of quantum computing is to design learning protocols that can outperform their classical counterparts [32, 33]. VQAs aim to tackle complex problems by integrating classical computation with NISQ devices — applications include determining energy spectra [34–37], simulating the Schrödinger equation [38–40], and advancing quantum machine learning techniques [18, 41, 42]. In this hybrid quantum-classical framework, classical computers optimize specific loss functions to identify optimal parameters, while the values and gradient information of these loss functions are obtained through measurements conducted on NISQ devices. This approach can significantly reduce the demand for quantum resources compared to ideal quantum computers [43].

In the fields of quantum chemistry [44] and many-body quantum systems [45], solutions to the Schrödinger equation are typically derived from standard large-scale eigenvalue problems, leading to the development of various methodologies aimed at

* Corresponding authors: Zhihao Lan (lanzhihao7@gmail.com); Jian Wei You (jvyou@seu.edu.cn); Tie Jun Cui (tjcui@seu.edu.cn).
† These authors contributed equally to this work.

tackling these challenges. Specifically, given the Hamiltonian of a quantum system, one can perform a classical optimization process on the loss function, where the minimum corresponds to the energy, and the associated state is interpreted as the approximate ground state. However, unlike standard eigenvalue problems [25, 34, 46–48], the challenge of employing quantum computing to address generalized eigenvalue problems [49–51] — which are pertinent to the band structure and eigenstate properties of photonic crystals — remains unresolved.

In this article, we propose a novel method for solving photonic crystal problems based on variational quantum algorithms, as illustrated in Fig. 1. We first derive the necessary generalized eigenvalue problem from Maxwell's equations using the finite-difference frequency-domain (FDFD) method [52–55]. Building upon this foundation, we construct a variational quantum generalized eigenvalue solver designed to compute the expected generalized eigenvalues efficiently. By devising an appropriate loss function and employing a quantum gradient descent algorithm, we successfully identify the minimum generalized eigenvalue. To validate our approach, we select two distinct photonic crystal structures situated in square and hexagonal lattices. The results demonstrate that a well-designed complex *Ansatz* yields quantum computational outcomes that closely align with classical numerical solutions, whereas a simpler *Ansatz* fails to provide accurate results, primarily due to the expressibility of fully parameterized quantum circuits being contingent on the complexity of the *Ansatz*. Utilizing ten qubits, we successfully achieve convergent solutions for the photonic crystals. Finally, we perform numerical simulations of our algorithm on a quantum cloud platform, yielding promising results that underscore the potential of our proposed method. Presently, VQAs exhibit considerable promise in various domains, including chemical simulation [56], molecular simulation [57], differential equation solving [58], computational fluid dynamics [59], and financial applications [60]. We are confident that this work will further propel the application value of such algorithms across a broader array of fields.

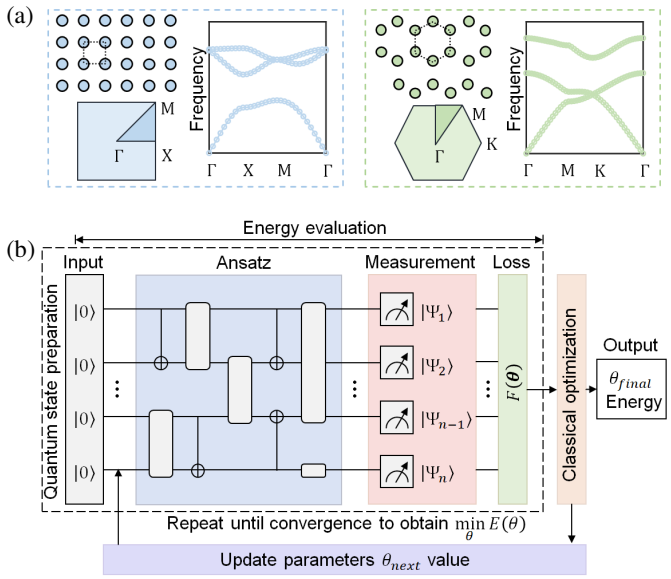

FIGURE 1. VQAs for PhCs. (a) Schematics of PhCs and their band structures. (b) N input qubits are processed through a quantum circuit, and the measured results are used to compute the loss function. A classical computer utilizes the gradient information obtained from the measurements to optimize and update the parameter set. This iterative process continues until the minimum is found, signaling the completion of the energy evaluation. Finally, the system outputs the desired eigenvalues.

2. GENERALIZED EIGENVALUE PROBLEM FOR PHCS

To derive the generalized eigenvalue equation for PhCs, we begin with Maxwell's equations. In a generalized coordinate system, the curl equations in free space can be expressed as:

$$\begin{cases} \nabla_q \times \hat{\mathbf{H}} = \imath k_0 \hat{\epsilon}\left(\mathbf{r}\right) \hat{\mathbf{E}} \\ \nabla_q \times \hat{\mathbf{E}} = -\imath k_0 \hat{\mu}\left(\mathbf{r}\right) \hat{\mathbf{H}} \end{cases} \tag{1}$$

where ∇_q is the differential operator in the generalized coordinate system, which is defined using three-unit vectors $\hat{u}_q(x, y, z)(q = 1, 2, 3)$. The use of generalized coordinate system aims to unify the treatment of different lattice symmetries: for a square lattice, the (x, y) coordinates are orthogonal; for a hexagonal lattice, it can be mapped to an oblique coordinate system (x', y') while maintaining the invariance of the equation's form. Specifically, the square lattice employs a standard orthogonal basis, while the hexagonal lattice is transformed into Cartesian space through a linear transformation of the generalized coordinates. Regardless of the geometric configuration of the lattice, the physical fields are defined in an experimentally measurable Cartesian coordinate system, with the generalized coordinates serving only as a mathematical tool for theoretical derivation. $\hat{\mathbf{E}}$ and $\hat{\mathbf{H}}$ denote the normalized electric and magnetic field vectors; k_0 is the wave number in free space; $\hat{\epsilon}$ and $\hat{\mu}$ represent relative permittivity and permeability, expressed in the form of 3×3 tensors.

In two-dimensional (2D) PhCs, because of the translational symmetry, the modes can be represented in Bloch form as:

$$\begin{cases} \mathbf{E}_{\left(n,k_z,\mathbf{k}_\parallel\right)}\left(\mathbf{r}\right) = e^{-i\mathbf{k}_\parallel\cdot\boldsymbol{\rho}} e^{-ik_z z} \mathbf{u}_{e\left(n,k_z,\mathbf{k}_\parallel\right)}\left(\boldsymbol{\rho}_1\right) \\ \mathbf{H}_{\left(n,k_z,\mathbf{k}_\parallel\right)}\left(\mathbf{r}\right) = e^{-i\mathbf{k}_\parallel\cdot\boldsymbol{\rho}} e^{-ik_z z} \mathbf{u}_{h\left(n,k_z,\mathbf{k}_\parallel\right)}\left(\boldsymbol{\rho}_1\right) \end{cases} \tag{2}$$

where n is the band index, and $\boldsymbol{\rho}_1$ indicates the mapping of the vector $\mathbf{r}$ onto the plane defined by (u_1, u_2). The periodic functions $\mathbf{u}_h(\boldsymbol{\rho}_1)$ and $\mathbf{u}_e(\boldsymbol{\rho}_1)$ satisfy the conditions $\mathbf{u}_h(\boldsymbol{\rho}_1) = \mathbf{u}_h(\boldsymbol{\rho}_1 + \mathbf{R})$ and $\mathbf{u}_e(\boldsymbol{\rho}_1) = \mathbf{u}_e(\boldsymbol{\rho}_1 + \mathbf{R})$, where $\mathbf{R}$ denotes a lattice vector.

In 2D PhCs, we focus on in-plane propagating modes ($k_z = 0$). Thus, the modes can be rewritten as:

$$\begin{cases} \mathbf{E}\left(\boldsymbol{\rho}_1\right) = e^{-i\mathbf{k}_\parallel\cdot\boldsymbol{\rho}_1} \mathbf{u}_e\left(\boldsymbol{\rho}_1\right) \\ \mathbf{H}\left(\boldsymbol{\rho}_1\right) = e^{-i\mathbf{k}_\parallel\cdot\boldsymbol{\rho}_1} \mathbf{u}_h\left(\boldsymbol{\rho}_1\right) \end{cases} \tag{3}$$

Consequently, Bloch's theorem can be expressed as

$$\begin{cases} \mathbf{E}\left(\boldsymbol{\rho}_1 + \mathbf{R}\right) = e^{-i\mathbf{k}_\parallel\cdot\mathbf{R}} \mathbf{E}\left(\boldsymbol{\rho}_1\right) \\ \mathbf{H}\left(\boldsymbol{\rho}_1 + \mathbf{R}\right) = e^{-i\mathbf{k}_\parallel\cdot\mathbf{R}} \mathbf{H}\left(\boldsymbol{\rho}_1\right) \end{cases} \tag{4}$$

Based on the Maxwell's curl Equation (1), we derive the governing equations for the PhCs modes:

$$\begin{cases} \nabla \times \hat{\mu}^{-1}(\mathbf{r}) \nabla \times \mathbf{E}(\mathbf{r}) = \omega^2 \hat{\epsilon}(\mathbf{r}) \mathbf{E}(\mathbf{r}) \\ \nabla \times \hat{\epsilon}^{-1}(\mathbf{r}) \nabla \times \mathbf{H}(\mathbf{r}) = \omega^2 \hat{\mu}(\mathbf{r}) \mathbf{H}(\mathbf{r}) \end{cases} \tag{5}$$

In 2D PhCs, the modes can be categorized into two polarizations: transverse magnetic (TM) modes and transverse electric (TE) modes. Here, we focus specifically on a periodic structure of air-silicon pillars in two dimensions, which satisfies two key assumptions: first, that the photonic crystal is invariant in the z direction, and second, that the dielectric tensor is diagonal. Based on these assumptions, the generalized eigenvalue matrix equations for TM and TE modes in 2D PhCs can be discretized as:

$$\begin{cases} \left\{U_1\left(\mu_{21}^{-1}V_2-\mu_{22}^{-1}V_1\right)-U_2\left(\mu_{11}^{-1}V_2-\mu_{12}^{-1}V_1\right)\right\}\hat{E}_z \\ =\varepsilon_{33}k_0^2\hat{E}_z \\ \left\{V_1\left(\varepsilon_{21}^{-1}U_2-\varepsilon_{22}^{-1}U_1\right)-V_2\left(\varepsilon_{11}^{-1}U_2-\varepsilon_{12}^{-1}U_1\right)\right\}\hat{H}_z \\ =\mu_{33}k_0^2\hat{H}_z \end{cases} \tag{6}$$

The computational domain is discretized into $n \times n$ points $A_{i,j}$ $(ij = 1 \ldots n)$.

$$\begin{cases} U_1 = \partial_x A_{x,y} \to (A_{i+1,j} - A_{i,j})/dx \\ U_2 = \partial_y A_{x,y} \to (A_{i,j+1} - A_{i,j})/dy \end{cases} \tag{7}$$

Here, we note that for U_1, it can be regarded as a composition of n blocks B $(n \times n)$, in which $B_{i,i} = -1$, $B_{i,i+1} = 1$ and $B_{n,1} = u_x$ in each individual block B, while for U_2, there exist $U^2_{i,i} = -1$, $U^2_{i,i+n} = 1$, and $U^2_{n(n-1)+i,i} = u_y$.

$$\begin{cases} V_1 = \partial_x A_{x,y} \to (A_{i,j} - A_{i-1,j})/dx \\ V_2 = \partial_y A_{x,y} \to (A_{i,j} - A_{i,j-1})/dy \end{cases} \tag{8}$$

Similarly, V_1 can be regarded as a composition of n blocks B, where $B_{i,i} = 1$, $B_{i+1,i} = -1$, and $B_{1,n} = v_x$ in each block B, while for U_2, there exist $V^2_{i,i} = 1$, $U^2_{i+n,i} = -1$, and $U^2_{i,i+n(n-1)} = v_y$.

The grid points on the boundaries are treated by the Bloch's theorem, expressed as:

$$\begin{cases} u_x = \exp(i\mathbf{k} \cdot a_1 \hat{\mathbf{u}}_1), \nu_x = -\exp(-i\mathbf{k} \cdot a_1 \hat{\mathbf{u}}_1) \\ u_y = \exp(i\mathbf{k} \cdot a_2 \hat{\mathbf{u}}_2), \nu_y = -\exp(-i\mathbf{k} \cdot a_2 \hat{\mathbf{u}}_2) \end{cases} \tag{9}$$

where a_1 and a_2 are the lengths of the unit cell in the respective directions. Based on this framework, we establish the generalized eigenvalue problem for PhCs.

3. VARIATIONAL QUANTUM GENERALIZED EIGENSOLVER

Based on (6), we obtain a standard generalized eigenvalue equation, with mathematical expression of the form:

$$A|\psi\rangle = \lambda B|\psi\rangle \tag{10}$$

where A is a Hermitian matrix, and B is a positive definite Hermitian matrix. For the TM mode, A and B are defined as follows: $A = U_1(\mu_{21}^{-1}V_2 - \mu_{22}^{-1}V_1) - U_2(\mu_{11}^{-1}V_2 - \mu_{12}^{-1}V_1)$, $B = \varepsilon_{33}k_0^2$. For the TE mode, A and B are defined as follows: $A = V_1(\varepsilon_{21}^{-1}U_2 - \varepsilon_{22}^{-1}U_1) - V_2(\varepsilon_{11}^{-1}U_2 - \varepsilon_{12}^{-1}U_1)$, $B = \mu_{33}k_0^2$. The eigenvector $|\psi\rangle$ corresponds to a generalized eigenvalue λ. The assumption here is that A and B can be decomposed as follows:

$$A = \sum_{m=0}^{M-1} \alpha_m A_m, \quad B = \sum_{n=0}^{N-1} \beta_n B_n \tag{11}$$

where A_m and B_n are unitary matrices. We also assume that the quantities M and N are polynomially related to the number of qubits, with p distinct generalized eigenvalues arranged in the increasing order.

It is noteworthy that the aforementioned decomposition is executed through Pauli decomposition. Specifically, we employ the SparsePauliOp tool provided by Qiskit to express A and B as linear combinations of Pauli operators, such that $A_m, B_n \in \{I, X, Y, Z\}^{\otimes L}$.

In order to estimate the minimum and maximum generalized eigenvalues, we select the following loss function, which can be interpreted as representing the first energy level of the PhCs, and perform a classical optimization process:

$$F(\boldsymbol{\theta}) = \frac{\mathrm{Tr}[AU(\boldsymbol{\theta})\rho U^\dagger(\boldsymbol{\theta})]}{\mathrm{Tr}[BU(\boldsymbol{\theta})\rho U^\dagger(\boldsymbol{\theta})]} \tag{12}$$

where $\rho = |\psi_{\text{in}}\rangle\langle\psi_{\text{in}}|$ is an arbitrary initial state of N qubits. The quantity $F(\boldsymbol{\theta})$ is viewed as the Rayleigh quotient corresponding to any state $|\psi(\boldsymbol{\theta})\rangle$, which is prepared by applying a parameterized quantum circuit $U(\boldsymbol{\theta})$ on the initial state $|\psi_{\text{in}}\rangle$ with adjustable gate parameters $\boldsymbol{\theta}$. For any state, we have

$$\lambda_1 = \min_{\theta} F(\boldsymbol{\theta}), \quad \lambda_p = \max_{\theta} F(\boldsymbol{\theta}) \tag{13}$$

where λ_1 and λ_p are associated with two optimal parameters $\boldsymbol{\theta}_1^*$ and $\boldsymbol{\theta}_p^*$, respectively.

When the matrix B is positive definite, the eigenvectors corresponding to different generalized eigenvalues are expressed as:

$$\langle\psi_i|B|\psi_j\rangle = \delta_{ij}, A|\psi_j\rangle = \lambda_j B|\psi_j\rangle \tag{14}$$

where δ_{ij} is the Kronecker delta function. Therefore, to obtain the other generalized eigenvalues and their corresponding eigenvectors, which are considered as the second and higher energy levels in the PhCs, we define a new loss function as follows:

$$F_j(\boldsymbol{\theta}) = F(\boldsymbol{\theta}) + \sum_{i=1}^{j-1} \gamma_i \mathrm{Tr}[BU(\boldsymbol{\theta})\rho U^\dagger(\boldsymbol{\theta}_i^*)]^2 \tag{15}$$

where $|\psi(\boldsymbol{\theta}_i^*)\rangle$ is the eigenvector that was previously determined, and γ_i is used in this work for subsequent optimization to obtain the corresponding minimum eigenvalue, ensuring that the minimum of the loss function corresponds to the j-th eigenvalue. It is important to note that this value only needs to be greater than the eigenvalue. In practice, we set it to a value significantly larger than the eigenvalue, as an excessively large

value does not prevent us from obtaining the optimization results. We consider that the loss function $F(\boldsymbol{\theta})$ is minimized under the constraint (i.e., $\mathrm{Tr}[BU(\boldsymbol{\theta})\rho U^{\dagger}(\boldsymbol{\theta}_i^*)]^2 = 0$). In this case, the j-th generalized eigenvalue and its associated eigenvector are given by

$$\begin{cases} \lambda_j = \min\limits_{\theta} F_j(\boldsymbol{\theta}) \\ |\psi_r(\boldsymbol{\theta}_j^*)\rangle = U(\boldsymbol{\theta}_j^*)|\psi_{\text{in}}\rangle \end{cases} \tag{16}$$

Thus, the last term of (15) represents the sum of inner products:

$$\mathrm{Tr}[BU(\boldsymbol{\theta})\rho U^{\dagger}(\boldsymbol{\theta}_i^*)]^2 = |\langle\psi(\boldsymbol{\theta})|B|\psi(\boldsymbol{\theta}_i^*)\rangle|^2 \tag{17}$$

It is noteworthy that we do not employ block encoding during measurement. Instead, we directly utilize the built-in functions of Qiskit, adhering to the standard process of the VQE, thereby avoiding the complexities associated with block encoding.

If we start with the initial state $|0\rangle = |0^{\otimes \log N}\rangle$, (17) can be further represented as:

$$\left|\sum_{n=0}^{N-1} \beta_l \langle \mathbf{0}|U^{\dagger}(\boldsymbol{\theta})B_n U(\boldsymbol{\theta}_i^*)|\mathbf{0}\rangle\right|^2 \tag{18}$$

The equation above represents the physical default state of a NISQ device (requiring no additional preparation gates). However, this does not hinder our theoretical derivation. In our actual simulations, we also utilize arbitrary random initial states as inputs, and there is no fundamental contradiction between the two approaches.

4. ANSATZ

4.1. Parameterized Quantum Circuits

The selection of an appropriate *Ansatz* is a crucial step. Generally, a fully parameterized quantum circuit structure offers significant flexibility, allowing for arbitrary quantum gate operations at each position. This structure primarily consists of various configurations of single-qubit and two-qubit gates. Here, we explore a range of *Ansatz* options and ultimately select two representative structures, as illustrated in Fig. 2: one is the simplest configuration, while the other is more complex. The former has been utilized in previous studies as a parameterized quantum circuit for training the tree tensor networks (TTN) and is composed of single-qubit rotation gates $R_y(\theta) = \exp(-\frac{i\theta Y}{2})$ and controlled NOT gates, enabling linear entanglement. The latter can represent a parameterization of arbitrary $SU(4)$ gate, composed of multiple rotation gates $R_y(\theta)$, $R_z(\theta)$, controlled NOT gates, and $U3(\theta, \phi, \lambda)$ gates. Because of its extensive parameter space and complex structure, this *Ansatz* possesses substantial computational power, making it suitable for nearly all problems, which is widely applied in quantum machine learning. A quantitative comparison of these two circuits can be found in Table 1.

It is important to note that while Circuit 2 yields superior results compared to Circuit 1, it significantly escalates the number of parameters that require optimization, thereby complicating the derivation of iterative gradient information from the loss function $F(\theta)$. This complexity represents one of the central challenges currently confronting the realm of variational quantum algorithms. While intricate parameterized structures (ansatz) can enhance expressive capacity, an excessive number of parameters often precipitates the phenomenon known as "Barren Plateaus," coupled with a substantial increase in the cost of classical optimization.

To address this issue, future research endeavors could focus on achieving a reduction in parameter scale through methods such as structural compression and parameter pruning. Specifically, we may adopt an adaptive approach to construct the ansatz, dynamically filtering for critical parameters instead of relying on a fixed structure of complex ansatz. Furthermore, by employing techniques for parameter importance assessment, we can eliminate superfluous parameters. These methodologies hold promise for significantly diminishing the number of parameters while ensuring the fidelity of the model, thus enhancing optimization efficiency and the practical applicability of the algorithm.

TABLE 1. Quantitative comparison of the two circuits under the condition (10 qubits).

Type	Parameters	Depth	Gates	Expressibility
Simple	72	4	36	Low
Complex	270	2	54	High

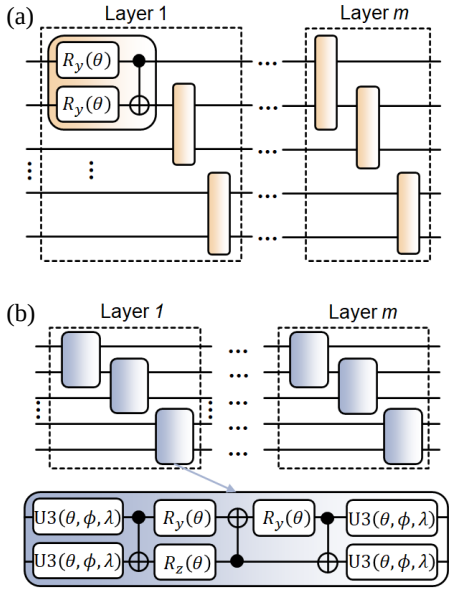

FIGURE 2. Parameterized quantum circuits. The *Ansatz* consists of m layers acting on an n-qubit register initialized in the computational basis. The rotation operation $R_i(\theta)$ represents a rotation by an angle θ around the i-axis of the Bloch sphere, while $U3(\theta, \phi, \lambda) = R_z(\phi) \cdot R_x(-\pi/2) \cdot R_z(\theta) \cdot R_x(\pi/2) \cdot R_z(\lambda)$ is a universal single-qubit gate (a) Structure of the simple Circuit 1. (b) Design of the more complex Circuit 2.

4.2. Implementation of the Proposed Algorithm

Here, we present our proposed algorithm for solving the generalized eigenvalue problem in PhCs. To effectively obtain dif-

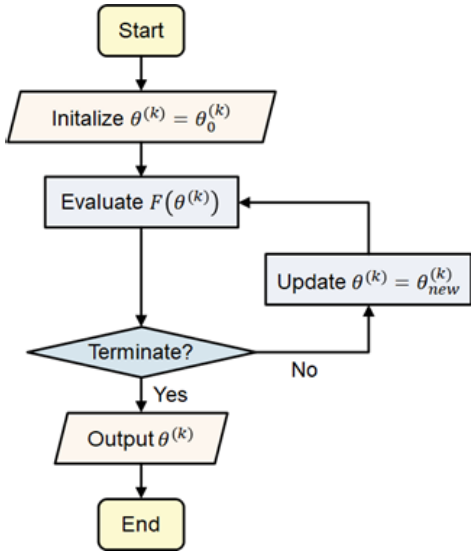

FIGURE 3. Flowchart describing our proposed algorithm. We carry out the above procedure in sequence.

ferent modes, we have devised a systematic algorithm. The detailed algorithmic workflow is illustrated in Fig. 3, which highlights the critical operations at each step. Through these steps, we are able to obtain photonic modes at various frequencies, allowing for an in-depth analysis of the optical properties and behaviors of PhCs.

Based on these two typical Ansatz options, the execution procedure of our algorithm is as illustrated in Algorithm 1.

5. NUMERICAL SIMULATIONS

We consider a 2D PhC composed of silicon ($\epsilon = 12\epsilon_0$) rods arranged in square and hexagonal lattices, with the rod radius of $0.11a$, where a is the lattice constant. We perform numerical simulations using VQAs to investigate the eigenproperties of PhC, including the band structure and corresponding eigenmode profile. In simulations, each point in the band structure requires a quantum variational iteration to be carried out. During the minimization process, we will update the circuit parameters θ in the iterative steps using a quantum gradient algorithm, with the resulting minimum energy representing a mode in the band structure.

For the first three bands of the hexagonal lattice, we execute the quantum variational algorithm 135 times, while for the square lattice, we perform it 96 times. Fig. 4 presents the computational results for a four-qubit circuit, in which each mode is obtained from the average of multiple runs. Compared to the classical solutions, the simulation results from Circuit 2 significantly outperform those from Circuit 1, primarily due to the enhanced expressibility of the Ansatz — specifically, the ability to explore the state space improves with the increase in the number of parameters. The electric field distribution further corroborates this observation. Here, we have selected two states for illustration; in fact, similar results are obtained for each state. It should be noted that in our circuit selection, we do not encounter the barren plateau problem. As shown in Fig. 5, we demonstrate that, for six different initial values, the eigenvalue

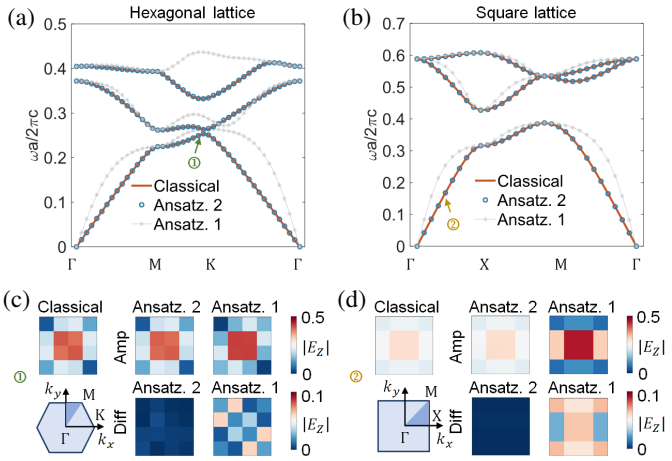

FIGURE 4. Numerical simulation results with four qubits. (a) Comparison of band structures for the hexagonal lattice and (b) the square lattice under two different *Ansatz* configurations. Comparison of electric field distributions for (c) the hexagonal lattice and (d) the square lattice using a representative mode. Note that $Diff = \sum |E_c - E_A|/E_c|$ where E_c and E_A represent the electric field amplitudes obtained from the FDTD and VQA methods, respectively. A smaller value of Diff indicates that the results obtained from our VQA method are closer to those from the classical FDTD calculations, signifying lower error and higher accuracy.

of the first energy level at the K point of the hexagonal lattice converges rapidly, remaining consistent with the FDTD results. We conduct extensive testing for various eigenvalues, each time achieving rapid convergence to the corresponding eigenvalue, which further underscores the strong convergence properties of our method.

Algorithm 1 Proposed algorithm for solving the generalized eigenvalue problem in PhCs

$\theta \leftarrow$ Random vector $\in [0, 2\pi)$
opt $\leftarrow$ Adam optimizer with $\eta = 0.01$
Precompute previous eigenstate parameters $\{\theta_i^*\}$
for t = 1 to Tmax do:
  E $\leftarrow \langle\psi(\theta)|\hat{H}|\psi(\theta)\rangle$
  P $\leftarrow \sum_i \gamma_i |\langle\psi(\theta)|B|\psi(\theta_i^*)\rangle|^2$
  L $\leftarrow$ E + P
  ∇L $\leftarrow$ Compute gradient via parameter shift
  $\eta_t \leftarrow$ Learning rate schedule
  $\theta \leftarrow$ opt.update (∇L, η_t)
  if $|L_t - L_{t-1}| < \varepsilon$ and $t > 200$ then break
end for
return $\lambda_j = L_t, \theta_j^* = \theta$

It is important to clarify that while the periodicity a does not affect the final band distribution (as our vertical coordinate represents relative values), in our actual simulations, the lattice constants of the two different lattices are both set to $a = 0.5\,\mu$m. The background medium is air, the rod radius is $0.11a$, and the grid resolution is set to 60×60. In both lattices, the selection of k paths must strictly match the lattice symmetry. The path for the square lattice is $\Gamma - X - M - \Gamma$, while the path for the hexagonal lattice is $\Gamma - K - M - \Gamma$, both following their respective Brillouin zones.

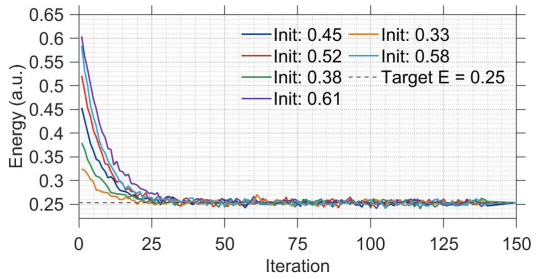

FIGURE 5. Convergence to the ground state energy (first band energy at K point of hexagonal lattice) under different initial values.

Specifically, in the square lattice, the first Brillouin zone is square-shaped. The coordinates of key high-symmetry points (with the lattice constant a) are as follows: Γ point (center of the Brillouin zone) $\Gamma = (0, 0)$, X point (center of the square edge) $X = (\frac{\pi}{a}, 0)$, and M point (vertex of the square) $M = (\frac{\pi}{a}, \frac{\pi}{a})$. The sampling points along the three segments of the closed path are 11, 12, and 11, respectively. In the hexagonal lattice, the first Brillouin zone is a regular hexagon. The coordinates of the key high-symmetry points are as follows: Γ point (center of the Brillouin zone) $\Gamma = (0, 0)$, K point (vertex of the hexagon) $K = (\frac{4\pi}{3a}, 0)$, and M point (center of the hexagonal edge) $M = (\frac{\pi}{a}, \frac{\pi}{\sqrt{3}a})$. The sampling points along the three segments of the closed path are 16, 15, and 16, respectively.

Figure 6 illustrates the relative differences $\delta = \frac{\sum \frac{\|\lambda^{VQA} - \lambda^{FDTD}\|}{\|\lambda^{FDTD}\|}}{N}$ between the results of VQAs and classical solutions for different numbers of qubits n, demonstrating a logarithmic convergence rate, where N represents the number of modes used for error calculation. The results indicate that as the number of qubits n increases from four to ten, the relative difference δ decreases by nearly two orders of magnitude, suggesting that increasing the number of qubits n will improve sampling efficiency and capture the mode variations more accurately. Furthermore, we conducted multiple independent initialization tests for different states, with the results showing

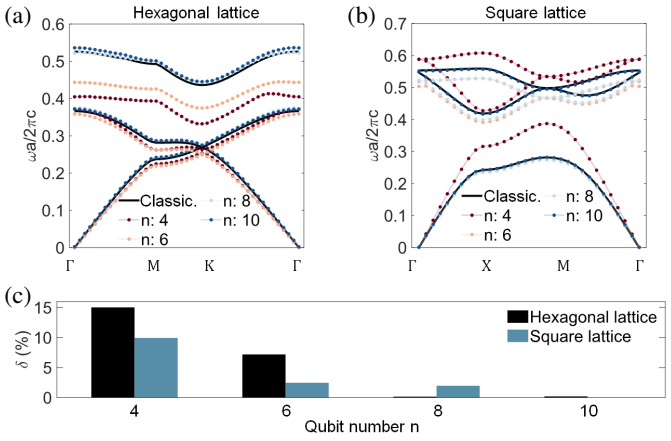

FIGURE 6. Effect of the number of qubits on the VQA results. Comparison of the obtained band structures for (a) the hexagonal and (b) square lattices at different numbers of qubits. (c) Variation of the relative difference between the results of VQAs and the classical results as the number of qubits increases.

that the 95% confidence interval for each state fluctuates approximately around 2×10^{-6}. The overall confidence interval also aligns with this range. This improvement is primarily due to the fact that n qubits can be mapped to a real-space grid of size 2^n, with a physical resolution of $2^{\frac{n}{2}} \times 2^{\frac{n}{2}}$. A denser grid division yields more precise results, consistent with the principles governing classical computations such as FDTD methods. It is noteworthy that we do not present results beyond 10 qubits. This is primarily because, in this study, regardless of the lattice structure employed, only 10 qubits are required for grid discretization to achieve results commensurate with classical solutions, thus obviating the necessity for additional qubits. Nonetheless, this limitation does not detract from the robustness of our findings, which convincingly validate the efficacy of the proposed methodology.

Furthermore, we provide a comparative analysis in Table 2 that details the results corresponding to different grid discretizations for varying numbers of qubits, focusing on the outcome of a characteristic value optimization process. It can be observed that when the number of qubits reaches 10 or more, the accuracy aligns closely with the results from FDTD numerical simulations, and we assume that this level of accuracy is satisfactory. Regarding computation time, it ranges from a few seconds to several hours as memory requirements also increase. However, regardless of the number of qubits used in the grid discretization, the results converge to the FDTD numerical results corresponding to the respective grid discretizations, rather than converging to the precise numerical solution of a very fine grid. Considering these factors, we ultimately chose to set the number of qubits to 10 to adequately meet the requirements. The interaction between discretization error and mesh partitioning constraints (i.e., the number of qubits) can be found in [61].

TABLE 2. Comparison results for different numbers of qubits.

Qubit number	Time(s)	Memory (MB)	Convergence	Accuracy
2	1.25	6028	✓	✘
4	6.23	6069	✓	✘
6	22.9	6079	✓	✘
8	91.5	6130	✓	✘
10	337.2	6324	✓	✓
12	1361.2	6692	✓	✓
14	5621.6	7116	✓	✓

To further validate the effectiveness of our approach, we present the electric field distributions of 96 distinct eigenmodes corresponding to the first three energy levels of square lattice PhCs, as illustrated in Figs. 7 to 10. These detailed visualizations provide a comprehensive overview of the behavior of the eigenmodes within the PhC structure. In this case study, we utilized a 10-qubit system for the computation, which allowed us to explore the complex interactions and patterns within the PhC lattice.

The results demonstrate a remarkable degree of consistency between our VQA and the numerical FDFD solutions under the

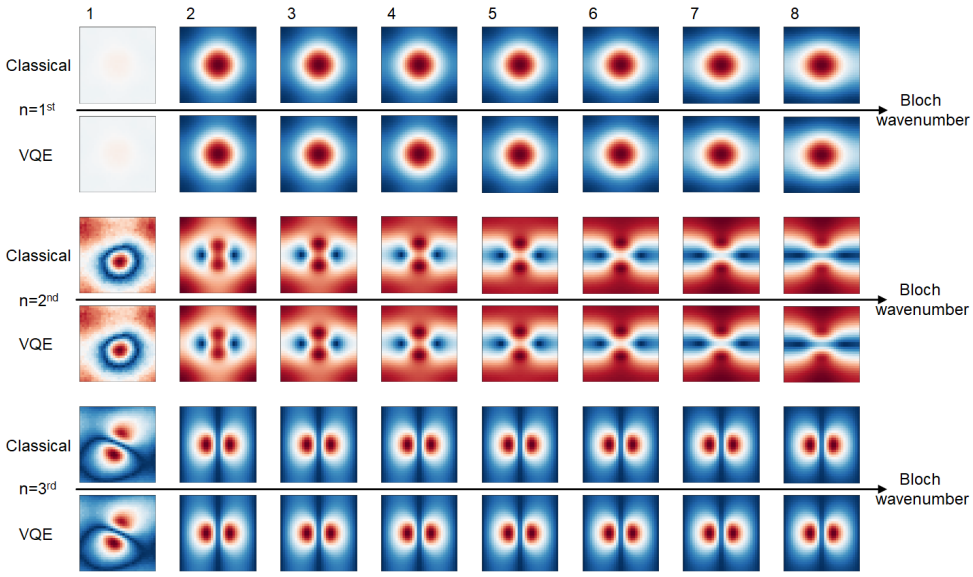

FIGURE 7. Comparison of the VQA method with the numerical FDFD solution for square lattices of the first three energy levels in the range of $k = 1$ to 8 at 10-qubits solution.

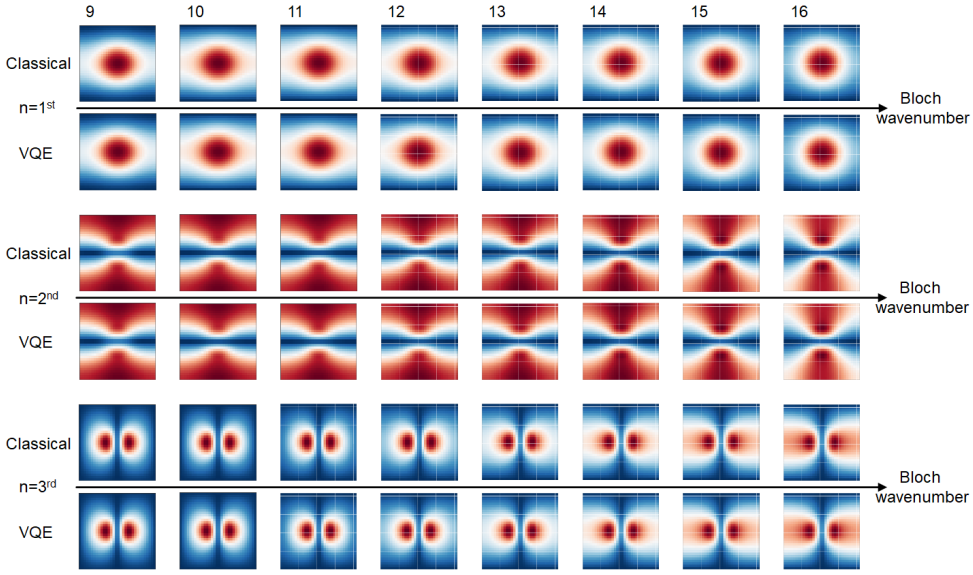

FIGURE 8. Comparison of the VQA method with the numerical FDFD solution for square lattices of the first three energy levels in the range of $k = 9$ to 16 at 10-qubits solution.

same grid discretization conditions. This high level of agreement not only proves the accuracy of our method in solving the eigenvalue problem of photonic crystals but also highlights its potential for addressing complex electromagnetic problems with high precision.

Moreover, we conducted a detailed analysis of the 19th mode of the second energy level to investigate the impact of the number of qubits on the accuracy of the solution. This analysis is presented in Fig. 11, which provides a comparative visualization of the results obtained with varying numbers of qubits under the same discretization conditions against the corresponding numerical FDFD solutions. At lower qubit counts, we observed significant discrepancies between the computed results and the correct electric field distributions. These differences are primarily attributed to the inherent inaccuracies in the grid discretization process, which can introduce errors when the computational resources (i.e., qubits) are limited. However, these discrepancies do not reflect any fundamental limitations of our proposed method but rather highlight the importance of sufficient computational resources for accurate simulations.

It is important to note that we do not directly encode spatial field values; instead, we treat the field distribution as an implicit property of the quantum state, extracting eigenvalues by measuring the expectation value of the Hamiltonian. The parameters of the rotation gates serve as classical variational parameters, and their optimization process is equivalent to searching

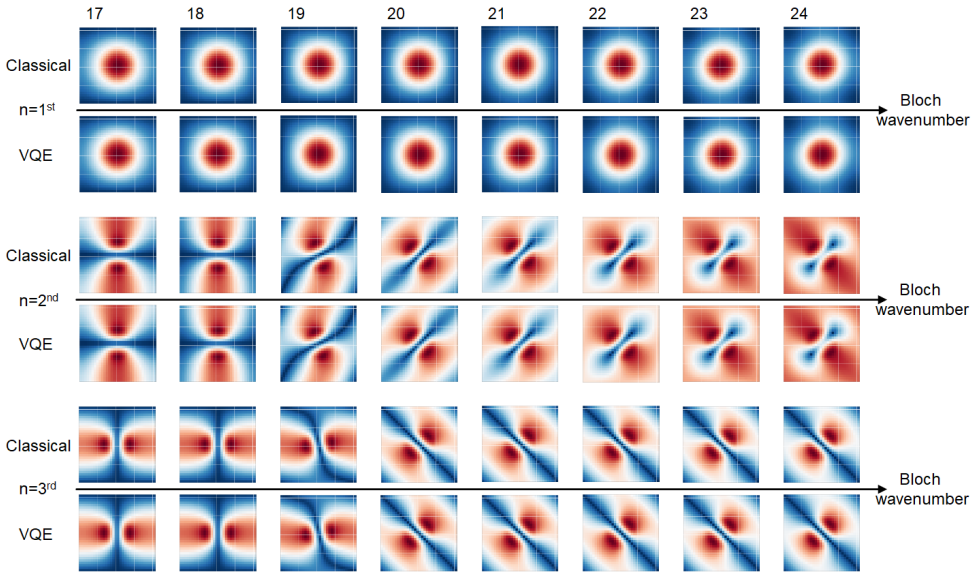

FIGURE 9. Comparison of the VQA method with the numerical FDFD solution for square lattices of the first three energy levels in the range of $k = 17$ to 24 at 10-qubits solution.

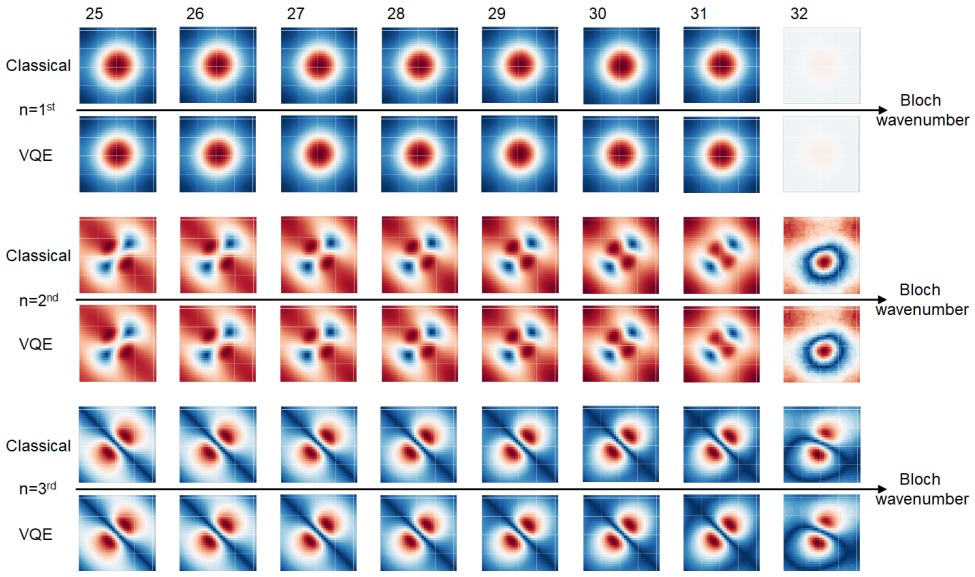

FIGURE 10. Comparison of the VQA method with the numerical FDFD solution for square lattices of the first three energy levels in the range of $k = 25$ to 32 at 10-qubits solution.

for a quantum state in Hilbert space that satisfies Maxwell's equations for the field distribution. This strategy effectively avoids the exponential resource consumption associated with continuous field encoding and represents an efficient solution to the eigenvalue problem.

Further observations reveal that as the number of qubits increases, the convergence of the algorithm is significantly enhanced. The computed results become increasingly close to the numerical FDFD solutions, demonstrating the scalability and robustness of our approach. This finding underscores the crucial relationship between the number of qubits and the accuracy of the algorithmic solutions. It suggests that with a sufficient number of qubits, our VQA can achieve highly accurate results that closely match the numerical FDFD solutions, even for more complex systems. It should be noted that our simulations utilized Qiskit version 1.1.0, which supports GPU acceleration. We employed the statevector simulator to avoid sampling noise, allowing for expectation values to be computed through precise matrix operations. We also omitted transpilation, directly mapping gate operations to unitary matrices while disregarding hardware topology constraints, and we did not implement error mitigation, simulating an ideal zero-noise environment. This work focuses on the design of quantum algorithms and their verification through classical simulations, hence we utilized Qiskit for ideal noise-free simulations. In the future, when quantum computers become practically viable, we can extend our approach to hardware for faster computations.

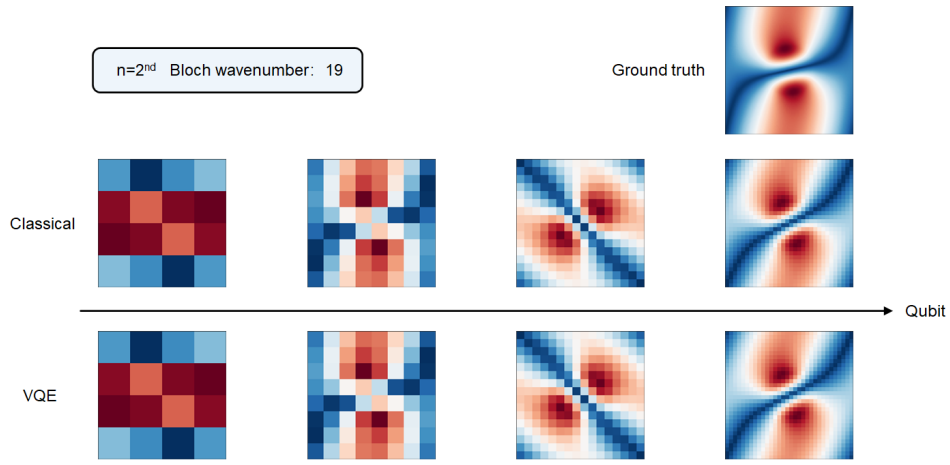

FIGURE 11. Comparison of VQA and numerical FDFD solutions for second energy level $k = 19$ mode with different qubit numbers.

Nevertheless, it is imperative to note that as the problem transitions from two-dimensional frameworks to more complex scenarios, such as three-dimensional photonic crystals, systemic challenges arise due to the proliferation of degrees of freedom, constraints posed by quantum hardware, and the complexity of algorithmic transitions. For instance, the demand for quantum bits will escalate, the complexity of Hamiltonian construction intensifies, the expressiveness of the ansatz encounters bottlenecks, and contradictions between parameter redundancy and insufficiency emerge, culminating in a rapidly increase in the iteration costs of the VQE, which includes heightened evaluation times for expectation values and increased burdens on optimizers. Additionally, issues related to the handling of boundary conditions, complexity of mode fields, and numerical stability necessitate further exploration. Consequently, future research should aim to incorporate advanced methodologies such as Quantum Natural Gradient (QNG) and Quantum Phase Estimation (QPE) to enhance the existing algorithmic framework.

6. CONCLUSION

In summary, this work successfully extends the application of VQAs to the investigation of PhCs by formulating a generalized eigenvalue problem grounded in Maxwell's equations. Through a comparative analysis of two distinct Ansatz quantum circuits, we conducted a comprehensive exploration of the band structure and eigenmode properties of the PhCs, which are critical for understanding their optical characteristics and potential applications in photonic devices. The complexity of the Ansatz was pivotal in enabling high-precision solutions for both square and hexagonal PhCs. Our findings illustrate that a well-structured Ansatz not only enhances the expressibility of quantum circuits but also improves the accuracy of the results. Moreover, we investigated the impact of qubit number on the accuracy of the solutions, thereby solidifying the validation of our method's precision and convergence. Importantly, the proposed algorithm is designed to be compatible with existing hardware, allowing for practical implementations in current quantum computing environments. Additionally, it can be integrated with quantum error mitigation techniques, which are crucial for enhancing the reliability of quantum computations in the presence of noise. Looking ahead, this methodology is poised for extension to problems such as the nonlinear Schrödinger equation [62], quantum phase transitions [63], and topological photonics, including topological phases protected by Floquet symmetry [64], associated topological states [65], as well as the precise ground states of Su-Schrieffer-Heeger open chains and Kitaev open chains [66]. This broadens the application prospects of VQA in both photonics and other fields, such as three-dimensional photonic crystals [67, 68] and photonic quantum devices [69, 70]. In particular, within the framework of nonlinear Maxwell's equations (such as Kerr media and second-harmonic generation), this algorithm can be expanded to address bistability and nonlinear mode coupling in photonic crystals through the variational encoding of nonlinear polarization operators. This provides a new computational paradigm for exploring soliton topology protection and frequency comb quantum dynamics, thereby broadening the application prospects of quantum computing in photonics and other fields.

Although this method demonstrates exceptional precision in ideal simulations, its practical deployment on NISQ hardware faces fundamental challenges that require systematic solutions. Firstly, gate fidelity errors constitute a major accuracy bottleneck, as the accumulation of errors in entangling gates can significantly distort the output state. Secondly, the strict budget on decoherence times imposes limitations on circuit depth, resulting in a significant gap from the optimal depth. Lastly, measurement errors can have a particularly detrimental impact on orthogonality penalty terms, potentially rendering the penalty mechanism ineffective. To address these challenges, we may need to adopt the following strategies in the future: (1) implementing dynamic decoupling sequences to extend the effective coherence time without disrupting the variational structure of the circuit; (2) combining zero-noise extrapolation (ZNE) with parameter shift rules; and (3) mitigating measurement errors by executing calibration circuits to obtain confusion matrices and applying Bayesian deconvolution to the orthogonality penalty terms.

APPENDIX A. OPTIMIZATION OF THE LOSS FUNCTION

To identify the optimal parameters $\{\boldsymbol{\theta}_i^*\}$, we employ a gradient-based optimization algorithm for random objective functions in variational quantum circuits. Additionally, gradient-free methods can also be applied for optimization. Starting from a randomly initialized parameter $\boldsymbol{\theta}^{(1)}$, the iterative update of parameters is given by:

$$|\boldsymbol{\theta}^{(s+1)} = \boldsymbol{\theta}^{(s)} - \delta \nabla F(\boldsymbol{\theta}^{(s)}) \tag{A1}$$

where δ is the learning rate, and $\nabla F(\boldsymbol{\theta}^{(s)})$ represents the gradient of the function $F(\boldsymbol{\theta})$ with respect to the parameter $\boldsymbol{\theta}^{(s)}$. Upon convergence, the optimal quantum circuit generates an approximate eigenstate $|\psi(\boldsymbol{\theta}^*)\rangle = U(\boldsymbol{\theta}^*)|\psi_{\text{in}}\rangle$, and the method discussed herein effectively avoids local minima.

To estimate the gradient of $F(\boldsymbol{\theta})$, we propose a universally applicable variational quantum circuit $U(\boldsymbol{\theta})$ constructed from single-qubit rotations and two-qubit entangling gates. Since the number of parameters scales linearly with the number of qubits and the circuit depth, a polynomial number of measurements is sufficient. The gradient of the loss function can be computed by rotating the parameter $\theta_t = (\theta_1^t, \ldots, \theta_n^t)^\dagger$, $t = 1, \ldots, M$ by π, which can be readily implemented on current quantum computers.

The gradients of the loss functions $F(\boldsymbol{\theta})$ and $F_j(\boldsymbol{\theta})$ can be estimated on recent quantum devices, provided that the operators $\frac{\partial U(\boldsymbol{\theta})}{\partial \theta_i^t}$ and $\frac{\partial U^\dagger(\boldsymbol{\theta})}{\partial \theta_i^t}$ can be effectively implemented on contemporary quantum computers. Specifically, the derivatives of $U(\boldsymbol{\theta})$ and $U^\dagger(\boldsymbol{\theta})$ with respect to a given angle θ_i^t can be obtained using the following formula

$$\frac{\partial U(\boldsymbol{\theta})}{\partial \theta_i^t} = \frac{1}{2} U(\boldsymbol{\theta}_+) \tag{A2}$$

$$\frac{\partial U^\dagger(\boldsymbol{\theta})}{\partial \theta_i^t} = \frac{1}{2} U^\dagger(\boldsymbol{\theta}_+) \tag{A3}$$

where $\boldsymbol{\theta} = (\theta_1^1, \ldots, \theta_i^t, \ldots)^\dagger$ and $\theta_+ = (\theta_1^1, \ldots, \pi + \theta_i^t, \ldots)^\dagger$.

This work also addresses the selection of the effective parameter γ_i in the loss function $F_j(\boldsymbol{\theta})$. Let $|\psi(\boldsymbol{\theta})\rangle := \sum_{i=1}^r a_i |\psi_i\rangle$ be the the trial state, and $|\psi_i\rangle$ is the i-th generalized eigenvector. We can choose $\gamma_i = \lambda_p - \lambda_1 > \lambda_j - \lambda_i$, where λ_p and λ_1 can be estimated by optimizing the loss function $F(\boldsymbol{\theta})$. It can be easily verified that:

$$\begin{aligned} F_j(\boldsymbol{\theta}) &= \frac{\sum_{i=1}^p |a_i|^2 \lambda_i}{\sum_{i=1}^p |a_i|^2} + \sum_{i=1}^{j-1} \gamma_i |a_i|^2 \\ &= \sum_{i=j}^{p} \left| |a_i|^2 \lambda_i + \sum_{i=1}^{j-1} (\gamma_i + \lambda_i) \right| a_i|^2 \\ &\geq \lambda_j \sum_{i=1} |a_i|^2 = \lambda_j \end{aligned} \tag{A4}$$

and if $\sum_{i=1}^p |a_i|^2 = 1$ and $\langle \psi_i | B | \psi_j \rangle = \delta_{ij}$, the first inequality yields:

$$\gamma_i + \lambda_i > \lambda_j \tag{A5}$$

Next, we provide further proof discussion. The unitary circuit $U(\boldsymbol{\theta})$ parameterized by $\boldsymbol{\theta}$ takes the following form:

$$U(\boldsymbol{\theta}) = \Pi_{t=M}^1 U_{ent} \left(\otimes_{i=1}^n R_y(\theta_i^t) \right) \tag{A6}$$

In this equation, $R_y(\theta_i^t) = e^{\frac{\mathrm{i}}{2}\theta_i^t Y}$ and $\boldsymbol{\theta} = (\theta_1^1, \ldots, \theta_1^M, \ldots, \theta_n^1, \ldots, \theta_n^M)^\dagger$. Thus, the derivative of $U(\boldsymbol{\theta})$ with respect to the parameter θ_i^t can be expressed as:

$$\begin{aligned} \frac{\partial U(\boldsymbol{\theta})}{\partial \theta_i^t} &= \Pi_{t=M}^1 U_e \otimes_{i=1}^n \frac{\partial R_y(\theta_i^t)}{\partial \theta_i^t} \\ &= \Pi_{t=M}^1 U_e \otimes_{i=1}^n \frac{-\mathrm{i}Y}{2} R_y(\theta_i^t) = \frac{1}{2} U(\boldsymbol{\theta}_+) \end{aligned} \tag{A7}$$

It is important to note that the above Equation (A7) provides the derivative of the quantum gate operator itself, describing the differential properties of the parameterized unitary operator. While this property is useful for theoretical derivations and operator computations, it is not aimed for gradient calculations in variational quantum algorithms. In actual implementations, the gradient of the expectation value follows the rule $\frac{\partial}{\partial \theta} \langle O \rangle_\theta = \frac{1}{2} \left(\langle O \rangle_{\theta + \pi/2} - \langle O \rangle_{\theta - \pi/2} \right)$. This represents the parameter shift rule used in variational quantum algorithms to compute the gradient of the objective function (expectation value) with respect to the parameters.

Additionally, we need to clarify that we are not shifting parameters for all gates; rather, we only need to shift the target gate because the angle being differentiated exists solely within a single gate, while the other gates remain unchanged. Moreover, the insertion position of the derivative term is strictly fixed; if the order is altered, it will completely change the physical meaning of the circuit. In this study, we utilize a ready-made automatic differentiation tool, which eliminates the need to consider gate order and operator insertion positions, effectively managing all product rules, gate sequences, and parameter identification issues.

The entangling gate is given by U_e with a sequence of CNOT gate applied on the qubit pair. The validity of the last equality is due to:

$$R_y(\pm\pi) = e^{\mp \frac{\mathrm{i}}{2}\pi Y} = \cos\frac{\pi}{2} I \mp \mathrm{i}\sin\frac{\pi}{2} Y = \mp \mathrm{i}Y \tag{A8}$$

$$\boldsymbol{\theta}_+ = (\theta_1^1, \ldots, \pi + \theta_i^t, \ldots)^\dagger \tag{A9}$$

Similarly, we can obtain expressions related to the first loss function:

$$\frac{\partial U^\dagger(\boldsymbol{\theta})}{\partial \theta_i^t} = \left(\frac{\partial U(\boldsymbol{\theta})}{\partial \theta_i^t} \right)^\dagger = \frac{1}{2} U^\dagger(\boldsymbol{\theta}_+) \tag{A10}$$

$$F(\boldsymbol{\theta}) = \frac{\langle \psi(\boldsymbol{\theta}) | A | \psi(\boldsymbol{\theta}) \rangle}{\langle \psi(\boldsymbol{\theta}) | B | \psi(\boldsymbol{\theta}) \rangle} = \frac{\langle A \rangle}{\langle B \rangle} \tag{A11}$$

$$\frac{\partial F(\boldsymbol{\theta})}{\partial \theta_i^t} = \frac{\partial}{\partial \theta_i^t} \frac{\langle A \rangle}{\langle B \rangle} = \frac{1}{\langle B \rangle^2} \left(\frac{\partial \langle A \rangle}{\partial \theta_i^t} \langle B \rangle - \langle A \rangle \frac{\partial \langle B \rangle}{\partial \theta_i^t} \right) \tag{A12}$$

It is evident that the inner product terms $\langle A \rangle$ and $\langle B \rangle$ can be computed using the Qiskit simulator Furthermore, the two additional terms, that is, $\frac{\partial \langle A \rangle}{\partial \theta_i^t}$ and $\frac{\partial \langle B \rangle}{\partial \theta_i^t}$ can be transformed into

a computationally favorable form. Specifically,

$$\frac{\partial \langle A\rangle}{\partial \theta_i^t} = \mathrm{Tr}\left[AU(\boldsymbol{\theta})\rho\frac{\partial U^\dagger(\boldsymbol{\theta})}{\partial \theta_i^t}\right] + \mathrm{Tr}\left[A\frac{\partial U(\boldsymbol{\theta})}{\partial \theta_i^t}\rho U^\dagger(\boldsymbol{\theta})\right] \tag{A13}$$

Substituting (A7) and (A10) into (A13), we obtain:

$$\frac{\partial\langle A\rangle}{\partial\theta_i^t} = \frac{1}{2}\begin{pmatrix} \mathrm{Tr}\left[AU(\boldsymbol{\theta})\rho U^\dagger(\boldsymbol{\theta}_+)\right] \\ +\mathrm{Tr}[AU(\boldsymbol{\theta}_+)\rho U^\dagger(\boldsymbol{\theta})] \end{pmatrix} \tag{A14}$$

$$\frac{\partial\langle B\rangle}{\partial\theta_i^t} = \frac{1}{2}\begin{pmatrix} \mathrm{Tr}\left[BU(\boldsymbol{\theta})\rho U^\dagger(\boldsymbol{\theta}_+)\right] \\ +\mathrm{Tr}[BU(\boldsymbol{\theta}_+)\rho U^\dagger(\boldsymbol{\theta})] \end{pmatrix} \tag{A15}$$

To compute the derivative of the loss function $F_j(\boldsymbol{\theta})$, we investigate the derivative of the additional term

$$\sum_{i=1}^{j-1}\gamma_i \mathrm{Tr}[BU(\boldsymbol{\theta})\rho U^\dagger(\boldsymbol{\theta}_i^*)]^2 \tag{A16}$$

$$\begin{aligned}&\frac{\partial}{\partial\theta_i^t}\sum_{i=1}^{j-1}\gamma_i \mathrm{Tr}[BU(\boldsymbol{\theta})\rho U^\dagger(\boldsymbol{\theta}_i^*)]^2 \\ &= 2\sum_{i=1}^{j-1}\gamma_i \mathrm{Tr}\left[BU(\boldsymbol{\theta})\rho U^\dagger(\boldsymbol{\theta}_i^*)\right]\mathrm{Tr}\left[B\frac{\partial U(\boldsymbol{\theta})}{\partial\theta_i^t}\rho U(\boldsymbol{\theta}_i^*)\right] \\ &= \sum_{i=1}^{j-1}\gamma_i \mathrm{Tr}[BU(\boldsymbol{\theta})\rho U^\dagger(\boldsymbol{\theta}_i^*)]\mathrm{Tr}[BU(\boldsymbol{\theta}_+)\rho U(\boldsymbol{\theta}_i^*)]\end{aligned} \tag{A17}$$

Consequently, the gradient of the loss function $F_j(\boldsymbol{\theta})$ is given by:

$$\frac{\partial F_j(\boldsymbol{\theta})}{\partial\theta_i^t} = \frac{\partial F(\boldsymbol{\theta})}{\partial\theta_i^t} + \frac{\partial}{\partial\theta_i^t}\sum_{i=1}^{j-1}\gamma_i \mathrm{Tr}[BU(\boldsymbol{\theta})\rho U^\dagger(\boldsymbol{\theta}_i^*)]^2 \tag{A18}$$

Another method for estimating the gradient is to use differential approximations, expressed as:

$$\frac{\partial F(\boldsymbol{\theta})}{\partial\theta_i^t} = \frac{F(\boldsymbol{\theta}+\Delta\theta) - F(\boldsymbol{\theta}-\Delta\theta)}{2\Delta\theta} \tag{A19}$$

where $\Delta\theta$ represents a small perturbation in the parameter $\boldsymbol{\theta}$. Generally, we hold $\Delta\theta$ fixed at a sufficiently small value. Finally, the gradients of the functions $F(\boldsymbol{\theta})$ and $F_j(\boldsymbol{\theta})$ have been computed on Qiskit simulator.

Finally, we would like to clarify that we employed a single optimizer strategy by directly utilizing the built-in Adam optimizer within the framework. This approach helps to avoid the uncertainties associated with custom implementations. To address the geometric characteristics of different energy level loss surfaces, we implemented a dynamic learning rate schedule (initialized at 0.01) to balance convergence and computational speed. For the ground state, we applied exponential annealing for rapid decay to prevent overshooting in convex optimization problems. For the excited states, we adopted a cyclic cosine annealing strategy with periodic restarts to facilitate traversal across saddle points and local minima. This strategy maintains the consistency of the optimizer while adaptively managing the complexity of the loss surfaces at different energy levels, achieving a balance between implementation simplicity and algorithm performance.

ACKNOWLEDGEMENT

This work was supported by the National Key Research and Development Program of China (No. 2023YFB3813100), National Natural Science Foundation of China (Nos. 62301149, 62101124, and 62288101), Natural Science Foundation of Jiangsu Province (Nos. BK20210209 and BK20230820), Special Fund for Key Basic Research in Jiangsu Province (No. BK20243015), 111 Project (111-2-05), Postdoctoral Innovation Talents Support Program under Grant BX20230066, Jiangsu Planned Projects for Postdoctoral Research Fund under Grant 2023ZB318, and China Postdoctoral Science Foundation (No. 2024M750418).

REFERENCES

[1] Schakel, A. M. J., "Relativistic quantum hall effect," *Physical Review D*, Vol. 43, No. 4, 1428, 1991.

[2] Qiu, R.-Z., S.-P. Kou, Z.-X. Hu, X. Wan, and S. Yi, "Quantum Hall effects in fast-rotating Fermi gases with anisotropic dipolar interaction," *Physical Review A — Atomic, Molecular, and Optical Physics*, Vol. 83, No. 6, 063633, 2011.

[3] Cage, M. E., R. F. Dziuba, and B. F. Field, "A test of the quantum Hall effect as a resistance standard," *IEEE Transactions on Instrumentation Measurement*, Vol. 34, No. 2, 301–303, 1985.

[4] Lee, T. Y., H. C. Koo, H.-J. Kim, S. H. Han, and J. Chang, "Electrical detection of the spin Hall effects in inas quantum well structure with perpendicular magnetization of [Pd/CoFe] multilayer," *IEEE Transactions on Magnetics*, Vol. 50, No. 1, 1–4, 2013.

[5] Kulig, M., P. Kurashvili, C. Jasiukiewicz, M. Inglot, S. Wolski, S. Stagraczyński, T. Masłowski, T. Szczepański, R. Stagraczyński, V. K. Dugaev, and L. Chotorlishvili, "Topological insulator and quantum memory," *Physical Review B*, Vol. 108, No. 13, 134411, 2023.

[6] Kang, Y., Y. Huang, and A. Z. Genack, "Dynamics of transmission in disordered topological insulators," *Physical Review A*, Vol. 103, No. 3, 033507, 2021.

[7] Crosse, J. A., S. Fuchs, and S. Y. Buhmann, "Electromagnetic Green's function for layered topological insulators," *Physical Review A*, Vol. 92, No. 6, 063831, 2015.

[8] Park, Y., Y. Park, H. Choi, S. Lim, D. Kim, and Y. Lee, "Tight-binding device modeling of 2-D topological insulator field-effect transistors with gate-induced phase transition," *IEEE Transactions on Electron Devices*, Vol. 71, No. 9, 5739–5743, 2024.

[9] Kosmanis, T. I. and T. D. Tsiboukis, "A systematic and topologically stable conformal finite-difference time-domain algorithm for modeling curved dielectric interfaces in three dimensions," *IEEE Transactions on Microwave Theory and Techniques*, Vol. 51, No. 3, 839–847, 2003.

[10] Haldane, F. D. M. and S. Raghu, "Possible realization of directional optical waveguides in photonic crystals with broken time-reversal symmetry," *Physical Review Letters*, Vol. 100, No. 1, 013904, 2008.

[11] Wang, Z., Y. D. Chong, J. D. Joannopoulos, and M. Soljačić, "Reflection-free one-way edge modes in a gyromagnetic photonic crystal," *Physical Review Letters*, Vol. 100, No. 1, 013905, 2008.

[12] Wang, Z., Y. Chong, J. D. Joannopoulos, and M. Soljačić, "Observation of unidirectional backscattering-immune topological electromagnetic states," *Nature*, Vol. 461, No. 7265, 772–775, 2009.

[13] Zeng, Y., U. Chattopadhyay, B. Zhu, B. Qiang, J. Li, Y. Jin, L. Li, A. G. Davies, E. H. Linfield, B. Zhang, Y. Chong, and

Q. J. Wang, "Electrically pumped topological laser with valley edge modes," *Nature*, Vol. 578, No. 7794, 246–250, 2020.

[14] Zhou, R., M. L. Chen, X. Shi, Y. Ren, Z. Yu, Y. Tian, Y. Liu, and H. Lin, "Protected transverse electric waves in topological dielectric waveguides," *IEEE Transactions on Antennas and Propagation*, Vol. 72, No. 2, 2058–2063, 2023.

[15] Ma, Q., L. Chen, S. L. Qin, X. Gao, Y. Zhang, S. Liu, J. W. You, and T. J. Cui, "Observing deformation-induced backscattering in flexible valley-Hall topological metasurfaces," *Advanced Optical Materials*, Vol. 13, No. 2, 2402078, 2025.

[16] Ma, Q., Z. Gu, X. Gao, L. Chen, S. L. Qin, Q. W. Wu, Q. Xiao, J. W. You, and T. J. Cui, "Intelligent hand-gesture recognition based on programmable topological metasurfaces," *Advanced Functional Materials*, Vol. 35, No. 1, 2411667, 2025.

[17] Qin, S. L., J. W. You, L. Chen, J. L. Su, Q. Ma, and T. J. Cui, "Phase-transition photonic brick for reconfigurable topological pathways," *Advanced Functional Materials*, Vol. 34, No. 48, 2408727, 2024.

[18] Benedetti, M., E. Lloyd, S. Sack, and M. Fiorentini, "Parameterized quantum circuits as machine learning models," *Quantum Science and Technology*, Vol. 4, No. 4, 043001, 2019.

[19] Bharti, K., A. Cervera-Lierta, T. H. Kyaw, T. Haug, S. Alperin-Lea, A. Anand, M. Degroote, H. Heimonen, J. S. Kottmann, T. Menke, W.-K. Mok, S. Sim, L.-C. Kwek, and A. Aspuru-Guzik, "Noisy intermediate-scale quantum algorithms," *Reviews of Modern Physics*, Vol. 94, No. 1, 015004, 2022.

[20] Cerezo, M., A. Arrasmith, R. Babbush, S. C. Benjamin, S. Endo, K. Fujii, J. R. McClean, K. Mitarai, X. Yuan, L. Cincio, and P. J. Coles, "Variational quantum algorithms," *Nature Reviews Physics*, Vol. 3, No. 9, 625–644, 2021.

[21] Endo, S., Z. Cai, S. C. Benjamin, and X. Yuan, "Hybrid quantum-classical algorithms and quantum error mitigation," *Journal of The Physical Society of Japan*, Vol. 90, No. 3, 032001, 2021.

[22] Du, Y., M.-H. Hsieh, T. Liu, S. You, and D. Tao, "Learnability of quantum neural networks," *PRX Quantum*, Vol. 2, No. 4, 040337, 2021.

[23] Huang, H.-Y., R. Kueng, and J. Preskill, "Information-theoretic bounds on quantum advantage in machine learning," *Physical Review Letters*, Vol. 126, No. 19, 190505, 2021.

[24] Colella, E., S. Beloin, L. Bastianelli, V. M. Primiani, F. Moglie, and G. Gradoni, "Variational quantum shot-based simulations for waveguide modes," *IEEE Transactions on Microwave Theory and Techniques*, Vol. 72, No. 4, 2084–2094, 2023.

[25] Ewe, W.-B., D. E. Koh, S. T. Goh, H.-S. Chu, and C. E. Png, "Variational quantum-based simulation of waveguide modes," *IEEE Transactions on Microwave Theory and Techniques*, Vol. 70, No. 5, 2517–2525, 2022.

[26] Ilin, Y. and I. Arad, "Dissipative variational quantum algorithms for gibbs state preparation," *IEEE Transactions on Quantum Engineering*, Vol. 6, 2025.

[27] Wurtz, J. and P. J. Love, "Classically optimal variational quantum algorithms," *IEEE Transactions on Quantum Engineering*, Vol. 2, 1–7, 2021.

[28] Huang, R., X. Tan, and Q. Xu, "Learning to learn variational quantum algorithm," *IEEE Transactions on Neural Networks and Learning Systems*, Vol. 34, No. 11, 8430–8440, 2022.

[29] Preskill, J., "Quantum computing in the NISQ era and beyond," *Quantum*, Vol. 2, 79, 2018.

[30] Zhou, Y., P. Zhang, and F. Feng, "Noisy-intermediate-scale quantum electromagnetic transients program," *IEEE Transactions on Power Systems*, Vol. 38, No. 2, 1558–1571, 2022.

[31] Khalid, U., J. U. Rehman, H. Jung, T. Q. Duong, O. A. Dobre, and H. Shin, "Quantum property learning for NISQ networks: Universal quantum witness machines," *IEEE Transactions on Communications*, Vol. 73, No. 4, 2207–2221, 2024.

[32] Biamonte, J., P. Wittek, N. Pancotti, P. Rebentrost, N. Wiebe, and S. Lloyd, "Quantum machine learning," *Nature*, Vol. 549, No. 7671, 195–202, 2017.

[33] Harrow, A. W. and A. Montanaro, "Quantum computational supremacy," *Nature*, Vol. 549, No. 7671, 203–209, 2017.

[34] Peruzzo, A., J. McClean, P. Shadbolt, M.-H. Yung, X.-Q. Zhou, P. J. Love, A. Aspuru-Guzik, and J. L. O'Brien, "A variational eigenvalue solver on a photonic quantum processor," *Nature Communications*, Vol. 5, No. 1, 4213, Jul. 2014.

[35] Higgott, O., D. Wang, and S. Brierley, "Variational quantum computation of excited states," *Quantum*, Vol. 3, 156, Jul. 2019.

[36] Jones, T., S. Endo, S. McArdle, X. Yuan, and S. C. Benjamin, "Variational quantum algorithms for discovering hamiltonian spectra," *Physical Review A*, Vol. 99, No. 6, 062304, Jun. 2019.

[37] Vogt, N., S. Zanker, J.-M. Reiner, M. Marthaler, T. Eckl, and A. Marusczyk, "Preparing ground states with a broken symmetry with variational quantum algorithms," *Quantum Science and Technology*, Vol. 6, No. 3, 035003, 2021.

[38] Li, Y. and S. C. Benjamin, "Efficient variational quantum simulator incorporating active error minimization," *Physical Review X*, Vol. 7, No. 2, 021050, 2017.

[39] Mahdian, M. and H. D. Yeganeh, "Incoherent quantum algorithm dynamics of an open system with near-term devices," *Quantum Information Processing*, Vol. 19, No. 9, 285, 2020.

[40] Endo, S., J. Sun, Y. Li, S. C. Benjamin, and X. Yuan, "Variational quantum simulation of general processes," *Physical Review Letters*, Vol. 125, No. 1, 010501, 2020.

[41] Wang, X., Z. Song, and Y. Wang, "Variational quantum singular value decomposition," *Quantum*, Vol. 5, 483, 2021.

[42] Li, K., S. Wei, P. Gao, F. Zhang, Z. Zhou, T. Xin, X. Wang, P. Rebentrost, and G. Long, "Optimizing a polynomial function on a quantum processor," *npj Quantum Information*, Vol. 7, No. 1, 16, 2021.

[43] LaRose, R., A. Tikku, Étude. O'Neel-Judy, L. Cincio, and P. J. Coles, "Variational quantum state diagonalization," *npj Quantum Information*, Vol. 5, No. 1, 57, 2019.

[44] Putterman, H., K. Noh, C. T. Hann, G. S. MacCabe, S. Aghaeimeibodi, R. N. Patel, M. Lee, W. M. Jones, H. Moradinejad, R. Rodriguez, *et al.*, "Hardware-efficient quantum error correction via concatenated bosonic qubits," *Nature*, Vol. 638, No. 8052, 927–934, 2025.

[45] Elhatisari, S., L. Bovermann, Y.-Z. Ma, E. Epelbaum, D. Frame, F. Hildenbrand, M. Kim, Y. Kim, H. Krebs, T. A. Lähde, D. Lee, N. Li, B.-N. Lu, U.-G. Meißner, G. Rupak, S. Shen, Y.-H. Song, and G. Stellin, "Wavefunction matching for solving quantum many-body problems," *Nature*, Vol. 630, No. 8015, 59–63, 2024.

[46] Mul, M., A. Lamecki, R. Gómez-García, and M. Mrozowski, "Inverse nonlinear eigenvalue problem framework for the synthesis of coupled-resonator filters with nonresonant nodes and arbitrary frequency-variant reactive couplings," *IEEE Transactions on Microwave Theory and Techniques*, Vol. 69, No. 12, 5203–5216, 2021.

[47] Liu, N., L. E. Tobón, Y. Zhao, Y. Tang, and Q. H. Liu, "Mixed spectral-element method for 3-D Maxwell's eigenvalue problem," *IEEE Transactions on Microwave Theory and Techniques*, Vol. 63, No. 2, 317–325, 2015.

[48] Wang, S. J., J. Liu, K. Chen, and Q. H. Liu, "A spurious-free domain decomposition method for 3-D Maxwell's eigenvalue problems," *IEEE Transactions on Microwave Theory and Techniques*, Vol. 71, No. 2, 548–560, 2023.

[49] Ford, B. and G. Hall, "The generalized eigenvalue problem in quantum chemistry," *Computer Physics Communications*, Vol. 8, No. 5, 337–348, 1974.

[50] Chugunova, M. and D. Pelinovsky, "Count of eigenvalues in the generalized eigenvalue problem," *Journal of Mathematical Physics*, Vol. 51, No. 5, 052901, 2010.

[51] Arroyo, J. and J. Zapata, "Subspace iteration search method for generalized eigenvalue problems with sparse complex unsymmetric matrices in finite-element analysis of waveguides," *IEEE Transactions on Microwave Theory and Techniques*, Vol. 46, No. 8, 1115–1123, 1998.

[52] Zhu, Z. and T. G. Brown, "Full-vectorial finite-difference analysis of microstructured optical fibers," *Optics Express*, Vol. 10, No. 17, 853–864, 2002.

[53] Guo, S., F. Wu, S. Albin, and R. S. Rogowski, "Photonic band gap analysis using finite-difference frequency-domain method," *Optics Express*, Vol. 12, No. 8, 1741–1746, 2004.

[54] Chen, M. L. N., L. J. Jiang, and W. E. I. Sha, "Generation of orbital angular momentum by a point defect in photonic crystals," *Physical Review Applied*, Vol. 10, No. 1, 014034, 2018.

[55] Fang, M., Z. Huang, W. E. I. Sha, and X. Wu, "Maxwell-hydrodynamic model for simulating nonlinear terahertz generation from plasmonic metasurfaces," *IEEE Journal on Multiscale and Multiphysics Computational Techniques*, Vol. 2, 194–201, 2017.

[56] Fedorov, D. A., B. Peng, N. Govind, and Y. Alexeev, "VQE method: A short survey and recent developments," *Materials Theory*, Vol. 6, No. 1, 2, 2022.

[57] Grimsley, H. R., S. E. Economou, E. Barnes, and N. J. Mayhall, "An adaptive variational algorithm for exact molecular simulations on a quantum computer," *Nature Communications*, Vol. 10, No. 1, 3007, 2019.

[58] Schillo, N. and A. Sturm, "Variational quantum algorithms for differential equations on a noisy quantum computer," *IEEE Transactions on Quantum Engineering*, Vol. 6, 1–16, 2025.

[59] Jaksch, D., P. Givi, A. J. Daley, and T. Rung, "Variational quantum algorithms for computational fluid dynamics," *AIAA Journal*, Vol. 61, No. 5, 1885–1894, 2023.

[60] Cong, T. N. N. and H. L. Thi, "Variational quantum algorithms in finance," in *Proceedings of Ninth International Congress on Information and Communication Technology*, 15–25, X. S. Yang, S. Sherratt, N. Dey, A. Joshi, (eds), Springer, Singapore, 2024.

[61] Joannopoulos, J. D., S. G. Johnson, J. N. Winn, and R. D. Meade, *Photonic Crystals: Molding the Flow of Light*, 2nd ed., 1–286, 2011.

[62] Köcher, N., H. Rose, S. S. Bharadwaj, J. Schumacher, and S. Schumacher, "Numerical solution of nonlinear Schrödinger equation by a hybrid pseudospectral-variational quantum algorithm," *Scientific Reports*, Vol. 15, No. 1, 23478, 2025.

[63] Cao, C., F. M. Gambetta, A. Montanaro, and R. A. Santos, "Unveiling quantum phase transitions from traps in variational quantum algorithms," *npj Quantum Information*, Vol. 11, No. 1, 93, 2025.

[64] Zhang, X., W. Jiang, J. Deng, K. Wang, J. Chen, P. Zhang, W. Ren, H. Dong, S. Xu, Y. Gao, F. Jin, X. Zhu, Q. Guo, H. Li, C. Song, A. V. Gorshkov, T. Iadecola, F. Liu, Z.-X. Gong, Z. Wang, D.-L. Deng, and H. Wang, "Digital quantum simulation of Floquet symmetry-protected topological phases," *Nature*, Vol. 607, No. 7919, 468–473, 2022.

[65] Sun, R.-Y., T. Shirakawa, and S. Yunoki, "Efficient variational quantum circuit structure for correlated topological phases," *Physical Review B*, Vol. 108, No. 7, 075127, 2023.

[66] Ciaramelletti, C., M. Beseda, M. Consiglio, L. Lepori, T. J. G. Apollaro, and S. Paganelli, "Detecting quasidegenerate ground states in topological models via the variational quantum eigensolver," *Physical Review A*, Vol. 111, No. 2, 022437, 2025.

[67] Cersonsky, R. K., J. Antonaglia, B. D. Dice, and S. C. Glotzer, "The diversity of three-dimensional photonic crystals," *Nature Communications*, Vol. 12, No. 1, 2543, 2021.

[68] Rinne, S. A., F. García-Santamaría, and P. V. Braun, "Embedded cavities and waveguides in three-dimensional silicon photonic crystals," *Nature Photonics*, Vol. 2, No. 1, 52–56, 2008.

[69] Holewa, P., D. A. Vajner, E. Zięba-Ostój, M. Wasiluk, B. Gaál, A. Sakanas, M. G. Mikulicz, P. Mrowiński, B. Krajnik, M. Xiong, K. Yvind, N. Gregersen, A. Musiał, A. Huck, T. Heindel, M. Syperek, and E. Semenova, "High-throughput quantum photonic devices emitting indistinguishable photons in the telecom C-band," *Nature Communications*, Vol. 15, No. 1, 3358, 2024.

[70] Crespi, A., R. Ramponi, R. Osellame, L. Sansoni, I. Bongioanni, F. Sciarrino, G. Vallone, and P. Mataloni, "Integrated photonic quantum gates for polarization qubits," *Nature Communications*, Vol. 2, No. 1, 566, 2011.